

Evidence for thermal-stress-induced rockfalls on Mars impact crater slopes

P.-A. Tesson^{a,b,*}, S.J. Conway^b, N. Mangold^b, J. Ciazela^a, S.R. Lewis^c, D. Mège^a

^a Space Research Centre, Polish Academy of Science, Wrocław, Poland

^b Laboratoire de Planétologie et Géodynamique UMR 6112, CNRS, Nantes, France

^c School of Physical Sciences, The Open University, Walton Hall, Milton Keynes MK7 6AA, UK

ARTICLE INFO

Keywords:

Mars, surface
Thermal stress
Ices
Solar radiation
Weathering

ABSTRACT

Here we study rocks falling from exposed outcrops of bedrock, which have left tracks on the slope over which they have bounced and/or rolled, in fresh impact craters (1–10 km in diameter) on Mars. The presence of these tracks shows that these rocks have fallen relatively recently because aeolian processes are known to infill topographic lows over time. Mapping of rockfall tracks indicate trends in frequency with orientation, which in turn depend on the latitudinal position of the crater. Craters in the equatorial belt (between 15°N and 15°S) exhibit higher frequencies of rockfall on their north-south oriented slopes compared to their east-west ones. Craters >15° N/S have notably higher frequencies on their equator-facing slopes as opposed to the other orientations. We computed solar radiation on the surface of crater slopes to compare insolation patterns with the spatial distribution of rockfalls, and found statistically significant correlations between maximum diurnal insolation and rockfall frequency. Our results indicate that solar-induced thermal stress plays a more important role under relatively recent climate conditions in rock breakdown and preconditioning slopes for rockfalls than phase transitions of H₂O or CO₂ at mid- and equatorial-latitudes. Thermal stress should thus be considered as an important factor in promoting mass-wasting process on impact crater walls and other steep slopes on Mars.

1. Introduction

Geomorphological processes are active at the surface of Mars at present day. Repeat-coverage and high resolution images (better than 50 cm/pix - McEwen et al., 2007) have revealed terrestrial-like gravitational mass movements (Tsige et al., 2016) ranging in size from landslides (Lucchitta, 1978) to single rockfalls (Roberts et al., 2012; Kumar et al., 2019). The spatial distribution of tracks left on slope-materials by falling rocks has been used as a passive seismometer on Mars and the Moon (Roberts et al., 2012; Kumar et al., 2016; Kumar et al., 2019). On Mars, few studies have been carried out investigating the factors that control rockfall activity. From single images alone, rockfalls appear to occur in a similar way as they do on Earth: a clast detaches from a cliff and rolls or bounces downslope, while leaving a track on the surface (Figs. 1 & 2A). However, weathering mechanisms leading to rockfall could differ substantially given the environment and climatic differences between Mars and Earth. For instance, liquid water plays a major-role in terrestrial slope stability (e.g., Terzaghi, 1962). The involvement of liquid water in active surface processes on Mars is widely debated (e.g., Schmidt et al., 2017; Ojha et al., 2017). Since liquid water

is generally not stable today on the martian surface (Farmer, 1976; Haberle et al., 2001; Hecht, 2002), it is unlikely, that water plays such an important role in slope instability on Mars as it does on Earth (Tsige et al., 2016).

On the other hand, Eppes et al. (2015) have linked boulder fracture patterns from Mars Exploration Rover (MER) Spirit images to directional solar-induced thermal stress on Mars. Further, on Earth, Collins and Stock (2016) showed that rockfalls can be linked to thermal stress. Therefore, we consider thermal stress as a potential weathering mechanism linked to rockfall activity on Mars at the present day. In order to evaluate its relative importance, we have catalogued recent rockfalls on the slopes of fresh impact crater walls across a range of latitudes to highlight different patterns of frequency, block size and orientation. Craters walls receive different amounts of insolation depending on their orientation and latitude. Therefore, they are exposed to relative differences of potential thermal stress intensity. If a link exists between thermal stress and rockfall activity, then they should have similar orientations.

* Corresponding author at: Space Research Centre, Polish Academy of Science, Wrocław, Poland.

E-mail addresses: pt@cbk.pan.wroc.pl (P.-A. Tesson), susan.conway@univ-nantes.fr (S.J. Conway), nicolas.mangold@univ-nantes.fr (N. Mangold), jc@cbk.pan.wroc.pl (J. Ciazela), stephen.lewis@open.ac.uk (S.R. Lewis), dmege@cbk.waw.pl (D. Mège).

<https://doi.org/10.1016/j.icarus.2019.113503>

Received 1 April 2019; Received in revised form 8 October 2019; Accepted 17 October 2019

Available online 26 October 2019

0019-1035/© 2019 Elsevier Inc. All rights reserved.

2. Theoretical background

2.1. Slope stability

Slope stability is a well-documented topic on Earth, especially in terms of geohazards related to landslides and rockfalls. Mechanically, a rockfall can be modelled as small-scale mass movement. It is a result of the breakup of an individual rocky object from the top of a slope (Selby et al., 1982). Fig. 1 outlines the factors that can contribute to a rockfall event.

Exposed rock (i.e. an outcrop) at the top of a topographic slope will be subject to gravity, and cohesion counteracts gravity’s pull resisting material failure and rockfall. A steep slope is the primary factor in controlling rockfall as the tangential component of the gravitational acceleration is a function of the slope angle. For failure to occur, the material needs to undergo a loss of cohesion as well. In a natural setting, environmental stresses lead to the growth of fractures via subcritical fracture that occurs due to stress magnitudes much lower than the critical strength of the rock (e.g. Eppes and Keanini, 2017). Over time, subcritical fracture growth results in loss of cohesion and reduction in material strength overall.

2.2. Longevity of rockfall tracks

Aeolian processes are active at the surface of Mars today (Bourke et al., 2008; Hansen et al., 2011) and study of the wheel tracks left by MER *Opportunity* and *Spirit* show that they persist for more than one martian year (Geissler et al., 2010; Sullivan et al., 2008). Rover tracks are susceptible to infill because they are located in areas where aeolian grains are easy to transport (Sullivan et al., 2008, 2005). On the other hand, rockfall tracks are located on sloping terrains, and may have slower infill rates because they are not exposed to the same aeolian transport mechanisms. To be conservative therefore we estimate that a meter-scale rockfall track could persist for more than a thousand years, and we acknowledge that this rate will vary from one context to another (aeolian activity, track depth and width, and substrate). Although this time period is short over geological timescales, orbital forcing related climate cycles are relevant (Laskar et al., 2004) and should be considered. We assume that if a track can still be observed, the rockfall should be recent and the weathering mechanism involved should still be ongoing at the surface today.

2.3. Thermal stress

High temperature contrasts experienced by rock surfaces in diurnal cycles lead to thermal expansion of the material at the surface, but less so at depth, and hence rock breakdown. This mechanism is widely studied on Earth. Rock breakdown linked to solar-induced thermal

stresses is known to occur in very arid environments in both cold (e.g. Antarctica, Lamp et al., 2017) and hot deserts (Hall, 1999; McKay et al., 2009; Eppes et al., 2010). Recent studies demonstrated that high stress can be correlated to high absolute maximum temperature and diurnal temperature range. These temperature parameters could thus be used as proxies of thermal stress (Boelhouwers and Jonsson, 2013; Collins et al., 2018; Eppes et al., 2016; Molaro and Byrne, 2012).

Thermal stress could cause rock breakdown on airless bodies (e.g. The Moon) (Molaro et al., 2015, 2017) as well as on Earth (Eppes et al., 2010; Warren et al., 2013). Therefore on Mars, arid conditions and high surface temperature gradients (e.g. Spanovich et al., 2006) suggest that thermoelastic stress might also occur on the surface at present day. Viles et al. (2010) were able to lower the strength of pre-stressed basaltic rocks under martian atmospheric conditions by exposing them to Mars-like diurnal cycles temperature variations. Based on boulder fracture patterns from *Mars Exploration Rover* (MER) *Spirit* images, Eppes et al. (2015) advocate active thermal stress-related rock breakdown. This directional relationship between thermal stress on Mars and the fracture patterns could exist also on rock walls. Growth of fractures caused by repetitive thermal stress cycles could lead to a fall, as known from Earth (Collins and Stock, 2016; Do Amaral Vargas et al., 2013; Gischig, 2016). If such a relation exists on Mars, there should be a correlation between number of rockfalls and maximum temperatures or/and maximum temperature ranges on slopes.

3. Material and methods

3.1. Site selection

Impact craters are widely distributed over the martian surface, and for that reason, can be used as sample locations to test the potential factors controlling rockfall distribution. Conveniently, they are circular allowing a relatively unbiased assessment of the influence of slope-orientation. Here, we focus on relatively fresh impact craters (Fig. 2B), from 1 to 10 km in diameter (Fig. 3) to reduce the influence of slope-inheritance from other long-term processes. Impact craters with a diameter < 10 km tend to have a “simple” bowl-shaped morphology, whereas craters with diameters > 10 km tend to have a more complex morphology (Melosh, 1989), including multiple wall terraces, which could complicate our analysis. Site selection was made by cross-referencing the global database of Mars impact craters from Robbins and Hynes (2012), and image data availability. Selected craters are located between 50°S and 40°N with most of them being located between 30°S and 30°N (Fig. 3) to avoid the latitude-dependent mantle (LDM). LDM is a meter-thick layer of ice and dust covering at least 23% of the surface that extends from the mid-latitudes to the poles (e.g. Conway and Balme, 2014; Kreslavsky and Head, 2002). It is a draping unit which likely formed during the many orbital variation-driven

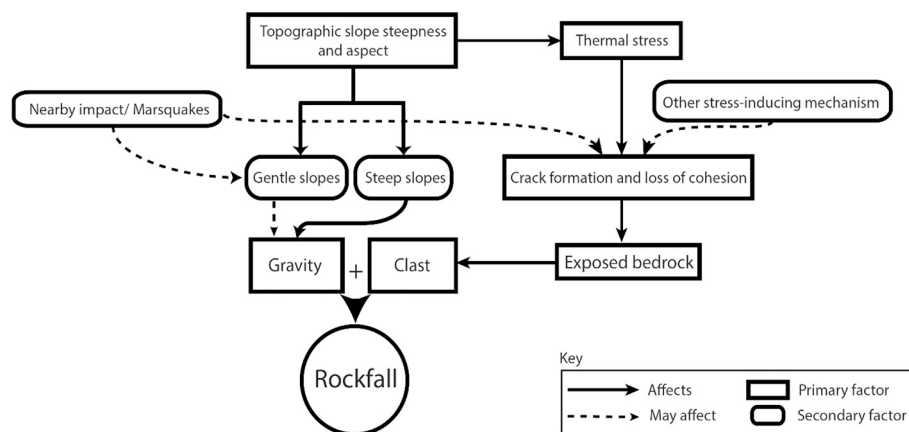


Fig. 1. Schematic diagram illustrating how thermal stress could influence rockfall activity. Firstly, a topographic gradient is needed. The slope value and orientation control the amount of insolation received by the surface, and hence the potential solar-induced thermal stress intensity. Energy is mostly provided by gravity, although marsquakes may also contribute (e.g. Roberts et al., 2012). A crack formation mechanism is required to weaken the exposed material and reduce its cohesion.

climate excursions that have occurred during the Amazonian period (Kreslavsky and Head, 2002). Fresh craters covered by LDM would introduce a bias in the results since LDM would tend to cover some of the slopes making rockfall tracks harder to observe, so we decided to discard craters where it was observed.

3.2. Dataset and mapping

Throughout this paper, we use the clast nomenclature suggested by Bruno and Ruban (2017). Because most of the clasts mapped in this study range from 1 to 10 m, we will refer to them as “blocks” as opposed to “boulders”, the term usually used, which refers to clasts smaller than 1 m in diameter according to this nomenclature.

In order to map rockfalls in impact craters, we have used images from *High Resolution Imaging Science Experiment* (HiRISE) instrument aboard the *Mars Reconnaissance Orbiter* (MRO), which provides a spatial resolution up to 0.25 m/pixel (McEwen et al., 2007) as listed in supplementary material, Table S1. Map-projected images were integrated in ArcGIS© 10.4 to identify and map recent rockfall tracks. We digitized the tracks left by the clasts as they fell (Fig. 2A) and where possible the long axis of block at the end of the track. From these polylines, we calculated their angle with respect to geographic north. For length measurements, we used a sinusoidal projection centered on the crater to reduce the distortion linked to map projection.

We used two different ways of evaluating frequency, using a normalized and a non-normalized representation for the distribution of rockfall track orientations. For both methods, we first calculated the number of rockfall tracks in 20° azimuth bins for each crater in a given latitude range. For the normalized distribution, we calculated for each crater the percentage of the total number of tracks in that crater for each azimuth bin. For each crater, the percentage of rockfalls in each bin is then relative to the number of rockfalls in the crater. We then calculated the mean percentage of tracks for each bin in all craters in this specific latitude range (Fig. 4, right). For the non-normalized distribution, the number of tracks in each bin was summed for every azimuth bin in each crater in each latitude set (Fig. 4 left), then the percentage is calculated relative to the total number of rockfall in the latitude range.

3.3. Topographic measurements

In order to assess variations in slope angle from crater-to-crater, or for different slope-orientations, for a sub-sample of our craters we examined the slope angle at the bedrock outcrops. Where it was possible, we generated Digital Terrain Models (DTM) at 24 m/pix from stereo-pairs of MRO Context camera (CTX) images at ~6 m/pix (Malin et al., 2007) using the *Ames Stereo Pipeline* (Broxton and Edwards, 2008). Before gridding, the generated point clouds were vertically controlled to Mars Orbiter Laser Altimeter (MOLA) elevation point data (PEDR) from

Mars Global Surveyor.

DTM accuracy was estimated by calculating the root mean square (RMS) between the elevation of the MOLA points and the mean elevation of the CTX DTM in a circle of 168 m in diameter surrounding those points. This diameter corresponds to the pulse diameter estimated from the point spread function (PSF) of MOLA instrument (Neumann, 2003). RMS results are reported in supplementary material, Table S2.

In order to estimate the slope of the crater wall outcrops, we split each crater into orientation bins, totaling 18 arc-segments each covering 20° of azimuth. In each bin, we extracted the elevation of every point between 50 and 200 m from the crater rim from where the clasts should typically fall from. This elevation range corresponds to where rock outcrops are generally observed (Conway et al., 2018), and may vary from a crater to another. We extract the slope value for each bin by taking the slope of a linear fit between the elevation and the distance from the rim for every DTM pixel (Fig. S1).

4. Results

We recorded 2040 recent rockfall tracks in 39 impact craters among which, 1584 tracks had an associated clast. Fig. 4 displays the frequency of rockfalls in craters with respect to the orientation of the crater wall, for different latitude ranges. Both the normalized and non-normalized plots show similar overall trends in each latitude range. The mid-latitude craters have the most rockfall tracks on the equator-facing slopes, in the northern and southern hemispheres. Northern mid-latitude craters have the highest number of rockfall tracks on the N-NE slopes (> 40% combined between N0° and N80°) in both normalized and non-normalized plots. S slopes have very few recorded rockfall tracks (< 20% in total from N100° to N260°) in both normalized and non-normalized plots. The mean vector inferred from these distributions is respectively $N13.3^\circ \pm 19.1$ and $N15.1^\circ \pm 19.6$ (95% confidence interval) for normalized and non-normalized distributions. Rayleigh and Rao’s test for the null hypothesis of uniformity yield P -value < .01 for the normalized distribution and 0.05 for the non-normalized distribution.

In the southern mid-latitudes, equator-facing slopes of craters have the most rockfall tracks. The normalized results show that up to 70% of the total number of rockfall tracks occur on the S slopes (i.e. north-facing, from N100° to N260°), whereas the non-normalized results only ~60% of total rockfall tracks occur in the same range. The non-normalized plot has larger percentage of rockfall tracks on the pole-facing slope (20% in total between N340° and N40°) than the normalized results (2–3% on average in the same bins). The mean vector inferred from these distributions is $N178.3^\circ \pm 27.6$ and $N141.6^\circ \pm 15.0$ (95% confidence interval) for the normalized and the non-normalized distribution, respectively. Rayleigh and Rao’s test for the null hypothesis of uniformity yield P -value < .01 in both cases.

At equatorial latitudes, there are more rockfall tracks on N-S-

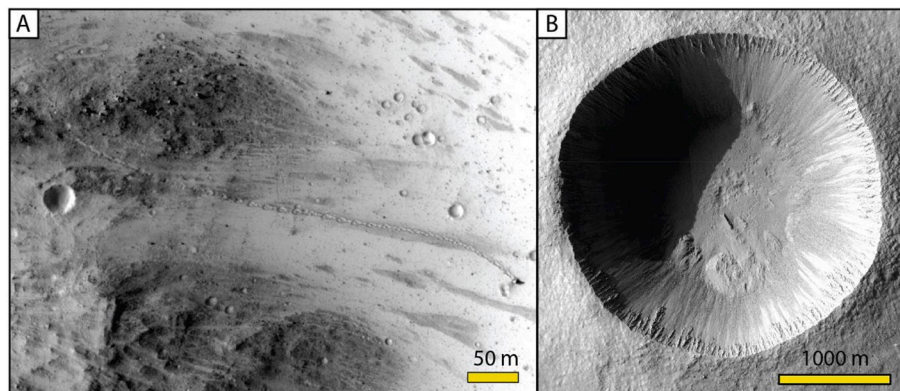


Fig. 2. A: An example of a recent rockfall displaying a clear track caused by rolling/bouncing with a clast at the end. HiRISE image: ESP_037190_1765. B: Zumba crater, a morphologically fresh impact crater representative of those used in this study. HiRISE image: PSP_002118_1510.

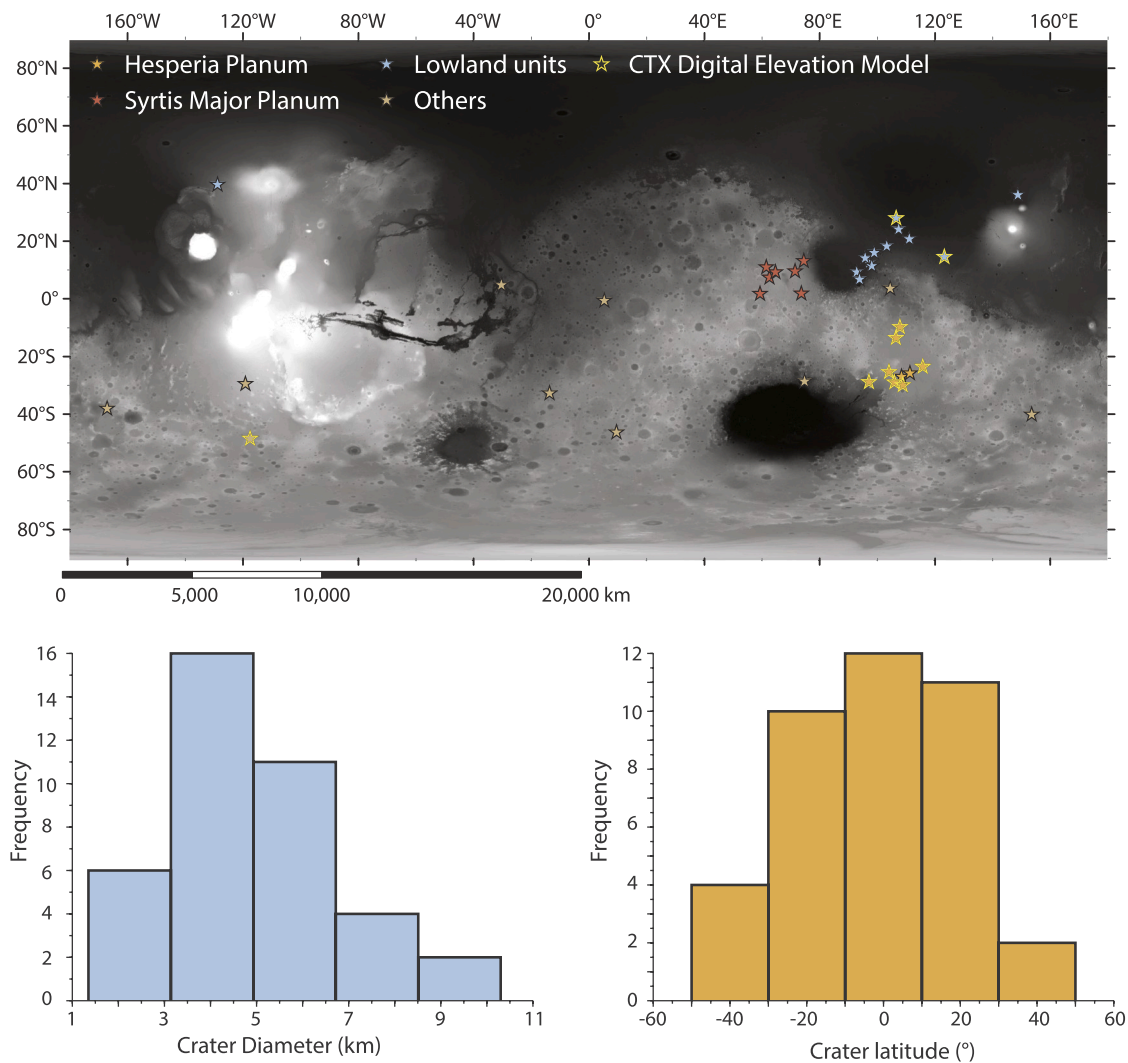


Fig. 3. Global distribution of 39 impact craters where fresh rockfall tracks and their associated clasts were mapped. **Bottom left:** The distribution of crater diameter for our sampled craters. **Bottom right:** The distribution of craters studied by latitude.

oriented slopes compared to E-W-oriented slopes. Specifically, the non-normalized distribution shows two peaks of 8% between N300°-N320° and N0°-N20°, and another one from N120° to N160° (15% combined). In the normalized distribution, the fraction of rockfall tracks is greater between N340° and N20° (18% combined) and from N180° to N200° (9%) compared to the non-normalized distribution. A peak in the N140°-N160° bin (7%) is also apparent in the normalized distribution. The mean vector is from N270° to N90° (northern slopes) is $N0.0^\circ \pm 12.9$ and $N322.5^\circ \pm 4.0$ for normalized and non-normalized distributions respectively, while it is $N176.6^\circ \pm 13.6$ and $N165.2^\circ \pm 4.0$ for the southern slopes, with a P-value $<.01$ in each case.

5. Rockfall clast size

5.1. Magnitude-frequency of rock volume

Fig. 5 shows the cumulative frequency-volume distribution of martian rockfalls mapped in this study.

Magnitude-cumulative frequency (MCF) distribution is commonly modelled by a power law in the middle section, with a deviation at the low and high sections (Corominas et al., 2017). The power-law exponent (referred to as “scaling parameter”) is thought to represent the fracture susceptibility of the rock mass under consideration. The scaling parameter of rockfalls in impact craters from our catalog is -1.23 .

On Earth, the scaling parameter of the power law usually varies from -0.90 to -0.40 , depending on geological, morphological and climatic conditions (Corominas et al., 2017), but also varies based on the technique used to measure the rock-dimensions. Using Terrestrial Laser Scanner (TLS)-generated 1 m/pix DTM to measure in-situ detachable rock volumes on a rock cliff (chute of Forat Negre, Andorra), Mavrouli et al. (2015) found an exponent of -1.3 while a previous study yielded a value of -0.9 (Santana et al., 2012) for the same investigated area when measuring rockfall scars with TLS. The higher value of the scaling factor for Mars compared to Earth could be explained by a difference in mapping method, but could also represent a difference in the rock mechanics between the two planets.

5.2. Median length of clasts

Fig. 6 shows the median long-axis length of rockfall clasts in each impact crater with respect to latitude and Fig. S2 the median long-axis length of rockfall clasts in each impact crater against crater diameter. The median size of recent rockfalls in the southern hemisphere is higher at the mid-latitudes than near the equator in Hesperia Planum and other locations on Mars (Fig. 6). The median size of blocks is >2.5 m at latitudes $>35^\circ$ S and decreases down to 2 m close to the equator. A weaker similar trend is observed in the northern hemisphere in Syrtis Major Planum and in the martian northern lowlands. To confirm whether this

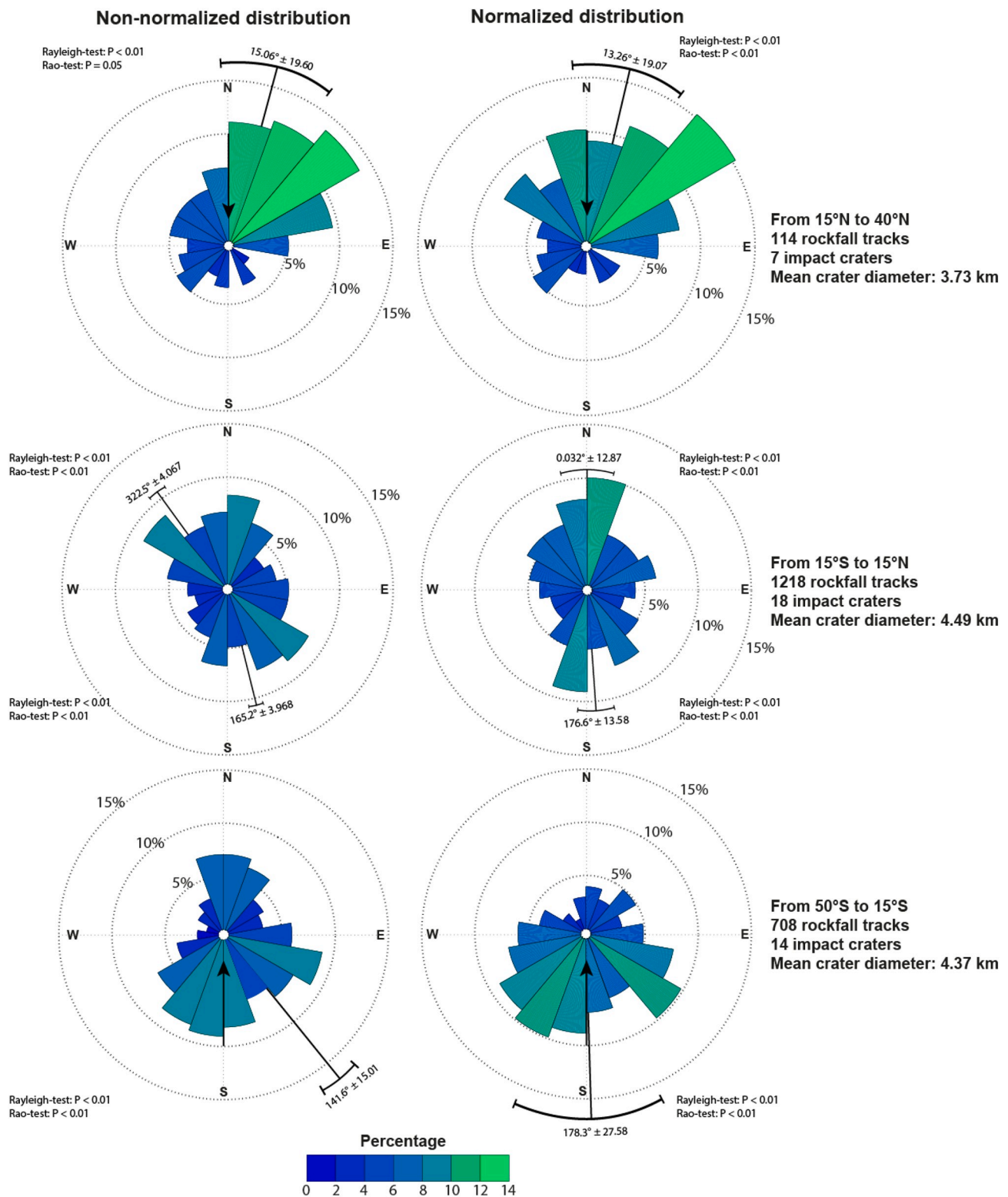


Fig. 4. Distribution of rockfall tracks by orientation in impact craters within different latitude ranges, derived using two different methods. All directions are with respect to the crater centers (e.g. North in the roses refers to northern slopes, i.e. south-facing, arrows indicate the direction to the equator). **Left:** non-normalized distributions, where the number of rockfall tracks in each orientation bin is summed for every crater in the specific latitude range and expressed as a percentage of the total number of rockfall tracks in this latitude range. This method emphasizes the signal from craters which have a large rockfall population (>100). **Right:** normalized distribution where the percentage of rockfalls is calculated for each orientation bin in each crater from which the mean is then derived for all craters in each latitude range. This method emphasizes the signal from craters having a relatively low rockfall population (<20). Lines correspond to vector means with 95% confidence interval depicted by brackets. Rao's spacing test and Rayleigh statistical test were performed for the null hypothesis of uniformity. Since equatorial plots display two distinct trends, we calculated two vector means for each half of the plots, assuming the other half is uniform.

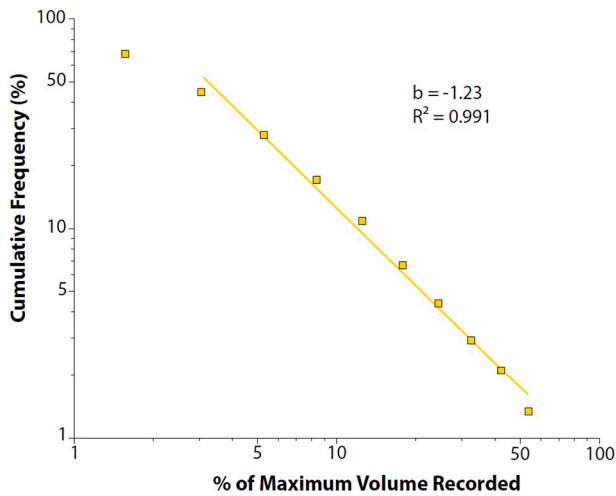


Fig. 5. Magnitude-cumulative frequency (MCF) relationship of clasts derived from martian rockfalls. Volume is calculated from the measured clast diameter by assuming an elliptical-shaped object with an aspect ratio of 0.8 (Kumar et al., 2019) and is normalized to the maximum volume recorded. A power-law fit is shown.

trend exists in the northern hemisphere more data would be needed >25°N.

6. Influence of slope on rockfalls

The sub-sample of ten craters with DTMs allows us to investigate the relationship between rockfall frequency and slope angle at the source. The aim of this analysis is to determine whether a systematic variation in slope angle with orientation and latitude could explain the frequency distribution of rockfall tracks reported in Fig. 4. These craters are equally distributed within the latitude range of our total sample set of 39 craters, and we find that >88% of rockfalls originate from slopes steeper than 32° (Fig. 7A).

Mars gravity is only 38% of Earth, therefore the question arises whether internal friction angle differs on Mars and Earth, where it is ~30°. Early experiments carried out by Viking landers have shown that angle of internal friction on Mars appears to be similar to typical Earth values, ranging from 27 to 39° (Moore et al., 1987). Therefore, the 32° value we found (Fig. 7A) is in line with expectations. The DTM resolution (24 m/pix) means we are measuring the overall slope value within the assumed rockfall source area, rather than the meter-scale slope from where the rocks detach.

The distribution of slope angle values follows a normal distribution for slopes with and without rockfalls (Fig. 7B). However, the distribution of slopes with rockfalls is shifted towards higher values of topographic gradient, in accordance with the expectation that increasing slope angle

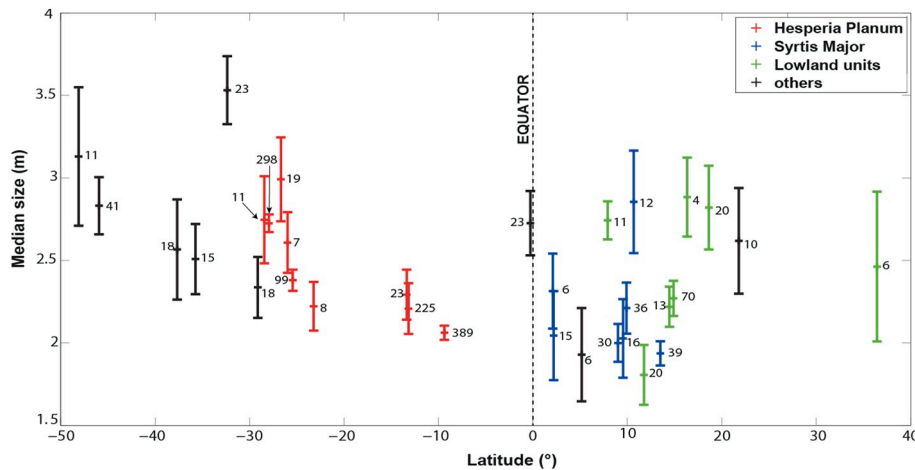


Fig. 6. Median long axis size of the rockfall clasts with respect of the latitude in each crater where recent rockfalls were mapped. The numbers next to each bar correspond to the number of clasts recorded in each crater. The error bars represent the standard errors. The craters with larger populations have lower standard errors. Craters are sorted by region to account for lithology variations, as different rock compositions would induce different thermal properties and thermal stress response.

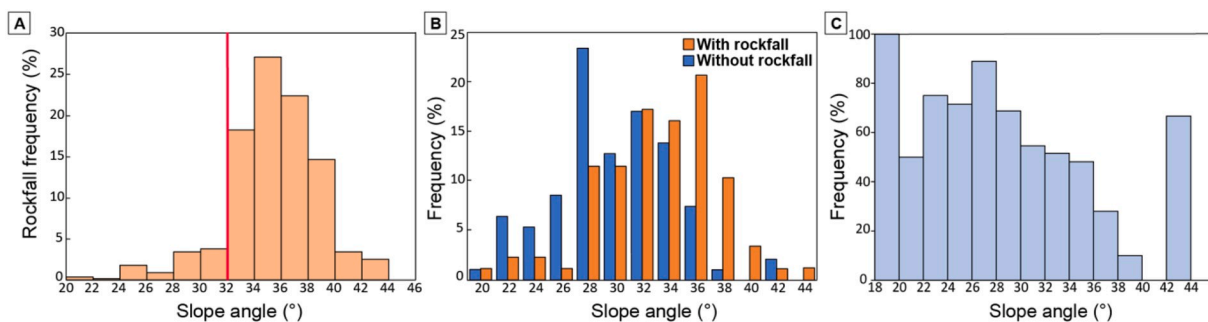


Fig. 7. Rockfall track frequency compared with slope derived from eleven digital terrain models. Slope is calculated for a 150 m wide area starting 50 m below crater rim, which is the most probable boulder source. Craters are divided into 20° bins in which rockfalls are counted. A slope value is attributed to each rockfall track, corresponding to the slope in the bin where it is located. **A:** Frequency of rockfall tracks against slope value. Rockfall tracks occur more frequently on slopes steeper than 32°. **B:** Frequency of all slopes with and without rockfall tracks. In both, the distribution is normal, but with different medians. **C:** Frequency distribution of slope angles for slopes without any observed rockfall tracks. 100% of slopes between 18 and 20° are devoid of rockfall tracks because they are not steep enough (Fig. 1). 28% of slopes between 36 and 38° do not display any rockfall tracks either. B and C highlight that a steep slope alone is not enough for a rockfall to occur, and that a stress-inducing mechanism is also necessary to promote loss of cohesion of the material (Fig. 1).

should increase rockfall activity (Fig. 1).

Mid-latitude equator-facing slopes on Mars are known to be steeper than pole-facing slopes (Kreslavsky and Head, 2003, 2018) and this could potentially explain the higher frequency of rockfalls on equator-facing slopes at our mid-latitude sites. The proposed explanation for this asymmetry is deposition and removal of the LDM (Kreslavsky and Head, 2018), although recent work has shown it could be related to enhanced glacial erosion on pole-facing slopes (Conway et al., 2018). Low-angle impact craters can display specific ejecta and interior morphologies (Herrick and Hessen, 2006), with a latitude-dependent frequency (Barlow and Bradley, 1990). Non-circular rim morphologies could create azimuthal variations in slope value in walls and influence rockfall activity.

Although rockfalls preferentially occur on steeper slopes, slope steepness alone does not condition rockfalls. Fig. 7C shows that a significant proportion of steep slopes do not have any rockfall tracks. For instance, 30% of 36–38° slopes have no rockfall tracks (Fig. 7C). Slopes angles of 42–44° slopes have no recorded rockfall tracks, but they only represent <2% of the population, meaning that this low proportion of rockfalls at steep slopes could be a statistical bias. Slopes steeper than 32° (excluding 42–44°) represent 27% of the measured population and have a proportion with rockfall tracks ranging from 52% to 10% (Fig. 7C). Therefore, if rockfall activity was dictated by topographic gradient only, the proportion of steep slopes with rockfalls should become closer to 100% the steeper the slope becomes. Such a correlation is not found in our results. Moreover, our impact craters are relatively fresh with a circular bowl-shaped morphology (Fig. 2B) and have been selected so to avoid influence of slope-inheritance from other long-term processes and LDM (see Section 3.1). Therefore, an anisotropic process must be involved in rock breakdown and rockfall activity on Mars at present-day to explain the observed frequency in occurrence of rockfall tracks in orientation with latitude (Fig. 4).

7. Other sources of rockfalls in impact craters

Ejecta blankets contain abundant clasts (ranging in size from silt to several ten-of-meter-large blocks) and can extend onto the upper interior walls of impact craters (Krishna and Kumar, 2016; Kumar et al., 2014). In addition, the ejecta layer is underlain by bedrock highly fractured during the impact (Kumar, 2005; Kumar and Kring, 2008). Both of those impact-related clasts are potential source of rockfalls in craters as they can simply fall due to gravity. However, the distribution of these rockfalls would be random, independent of slope orientation, which is in contrast with our highly oriented distributions. (Fig. 4).

As impact craters in this study are relatively young, they also could be exposed to ongoing modification process such as impact crater collapse (Melosh and Ivanov, 1999) which could be the source of rockfalls. This factor, however, should also act randomly and is not expected to cause any latitude-dependent orientation pattern of rockfall on crater walls.

At mid-latitudes (>30°), crater walls may display gullies that could be a source of rockfalls (Harrison et al., 2015). However, gullies between 30° and 40° prevail on the pole-facing slopes (Conway et al., 2019) while rockfalls seem to occur preferentially on equator-facing slopes at those latitudes (Fig. 4). One could also argue that gullies have the opposite effect and tend to reduce rockfall activity, or simply introduce a bias in the mapping itself by reducing their visibility. However, this would cause lower detection of rockfalls on craters at >30° latitudes, which is not the case. Our data indicate relatively constant rockfall frequency from 15° to 40/50° in both hemispheres (Fig. 4).

8. Marsquakes and other triggers

Although most of the energy needed for rockfall is provided by gravity, loss of material cohesion may not be sufficient to trigger rockfall. Other local sources of energy could play this role.

Rockfall activity has been used to infer present-day seismic activity on Mars and on the Moon (Roberts et al., 2012; Kumar et al., 2016; Brown and Roberts, 2019). During earthquakes, energy decreases with distance from epicenter. Keefer (1984) noted that spatial frequency and intensity of slope instabilities increase closer to earthquake epicenter. For instance, Roberts et al. (2012) reported an increase in clast size and spatial distribution of recent block falls on along *Cerberus Fossae* floor around a specific location and exclude other triggering factors than recent marsquakes. Marsquakes could thus also affect the rockfall distribution observed here. In addition, rockfalls may be caused by neighbouring impacts or by wind. All in all, however, such phenomena should only occur locally and could not explain the systematic patterns with latitude observed here (Fig. 4).

9. Weathering mechanism

9.1. Phase changes of ice

On Earth, the phase change of water from liquid to solid is usually responsible for rock-breakdown and can result in rockfall. Freezing and thawing are rare on Mars as liquid water is unstable under current atmospheric conditions (average pressure of 6 mbar - Farmer, 1976; Haberle et al., 2001; Hecht, 2002) although special regions have been identified where this could happen (e.g. Chevrier et al., 2009) and availability of metastable liquid water is thought to affect weathering rate, even during the late Amazonian period (De Haas et al., 2013).

Compared to liquid water, water ice is abundant on Mars and the ice itself can change volume and can produce stresses of >5 MPa (Mellon, 1997). Hence, rock may be broken down by seasonal and/or diurnal thermal contraction of ice. Ground ice is thought to exist from the mid to high latitudes (>45°) on modern Mars, and has been documented in multiple locations using both orbital (Boynton et al., 2002; Byrne et al., 2009; Dundas et al., 2018; Mouginot et al., 2010) and in-situ data (Mellon et al., 2009). Also, ground H₂O ice is inferred to exist from the observed distribution of CO₂ seasonal ices on pole-facing crater slopes at latitudes as low as 25° in the southern hemisphere (Vincendon et al., 2010a).

In addition to water, CO₂ seasonal frost resulting from condensation of atmospheric CO₂ in winter is known to form a continuous >10 g/cm² layer which extends from polar caps to 60° in latitude in both hemispheres (James et al., 2005; Kelly et al., 2006). Small patches of seasonal frost can also be found in shadowed pole-facing slopes at latitudes as low as 33°S with modelled concentration reaching 8 g/cm² (Schorghofer and Edgett, 2006). Thin layers (<1 mm) of diurnal CO₂ frost also exists at low latitude, down to the equator, on low thermal inertia, dusty units (Piqueux et al., 2016).

Small concentrations of water ice are associated with CO₂ frost, even at mid-latitudes (Schorghofer and Edgett, 2006; Carrozzo et al., 2009; Vincendon et al., 2010b) and surface H₂O ice frost deposits were observed by the Viking lander 2 at 47.64°N (Farmer, 1976). Vincendon et al. (2010b) observed water ice deposits ranging from 2 to 200 μm at latitudes as low as 13°S and 32°N combining data from imaging spectrometers and a modeling approach. These thin deposits are derived from atmospheric humidity (recorded in TES data - Smith, 2002) generated by sublimation of ground water ice and polar caps. Higher relative humidity itself can also increase crack growth velocity (Nara et al., 2017). Relative humidity is greater for a higher water vapour content and a lower temperature (Harri et al., 2014), meaning crack growth velocity should be highest at the mid-latitudes and above, where the atmospheric water content is greater (Smith, 2002) and temperatures lower.

Martian rockfalls linked to phase changes of H₂O and CO₂ should occur where these ices are expected to condense and/or be preserved from previous ice ages, namely on pole-facing slopes in the mid- to high-latitudes and rarely at the equator. Our results show that rockfalls occur on equator-facing slopes both in the mid- and equatorial-latitudes

(Fig. 4), suggesting that phase changes of H₂O and CO₂ are not involved.

9.2. Solar radiation model

The latitude-dependence of rockfall orientations indicates that insolation plays a role in the source-rock breakdown and the preconditioning for rockfall occurrence on impact crater slopes. For this reason, thermoelastic stress is likely to play a role.

To assess the variation in insolation with latitude, we computed solar insolation over a typical DTM of a crater placed at different latitudinal positions. We used the publicly available HiRISE DTM (DTEEC_002118_1510_003608_1510_A01) of Zumba crater (Fig. 2B & S3) to represent a typical fresh crater. The DTM was reduced to 10 m per pixel and we only considered the crater walls to achieve a reasonable tradeoff between resolution and computation time. For each pixel, a “viewshed”, which provides information on the sky visibility in every direction, is first derived from the DTM (Rich et al., 1994). The model then computes solar incidence angle of each pixel with respect to slope angle and orientation, and sun position in the sky at a given moment. We ran the model for a martian day (sol) every 10° of solar longitude (Ls) for the whole martian year. For each sol, direct insolation in W/m² is computed every half hour of local time. The daily mean is then calculated by averaging the solar flux at each step for the entire sol. Equations making up the mathematical framework of our model are all extracted from Appelbaum and Flood (1990). Details on the model are available in Appendix A. We obtained a raster that represents the maximum diurnal average insolation received by the crater walls at a given latitude over a martian year.

9.3. Orbital parameters

The lifetime of the tracks left by rockfalls could be up to several tens of thousands of years (see Section 2.2). This timescale requires that changes in orbital parameters be considered when studying latitude-dependent processes depending on insolation. During the last 100,000 Mars years, the eccentricity of Mars’ orbit has ranged from 0.075 to 0.118, being 0.093 today (Laskar et al., 2004). Eccentricity influences seasonal contrasts, and therefore it is unlikely to play a role in the relative rates of weathering for different slope orientations at different latitudes. In the same period the obliquity has ranged from 22.5° to 26.8° (25.2° today - Laskar et al., 2004), which is likely too small to have any noticeable effect on the insolation patterns per orientation with latitude. However, during the same period, Mars has experienced two full precession cycles, implying that the solar longitude at which perihelion occurs has changed significantly. For instance, 22,700 years ago, Mars’ perihelion occurred at Ls = 90° (Laskar et al., 2004), meaning that maximum insolation was received during northern summer (Fig. 8) and solar insolation was at its yearly maximum on north-facing slopes at the equator. This is the opposite of the situation today. With perihelion at Ls = 90°, north-facing slopes at the equator would experience maximum diurnal and seasonal temperature contrasts, as is currently the case for south-facing slopes. Precession cycles should therefore be considered when computing insolation received by crater slopes during the last 100,000 Mars years. For each crater, we have computed maximum diurnal average insolation for specific values of solar longitude of perihelion to estimate the average over a full precession cycle.

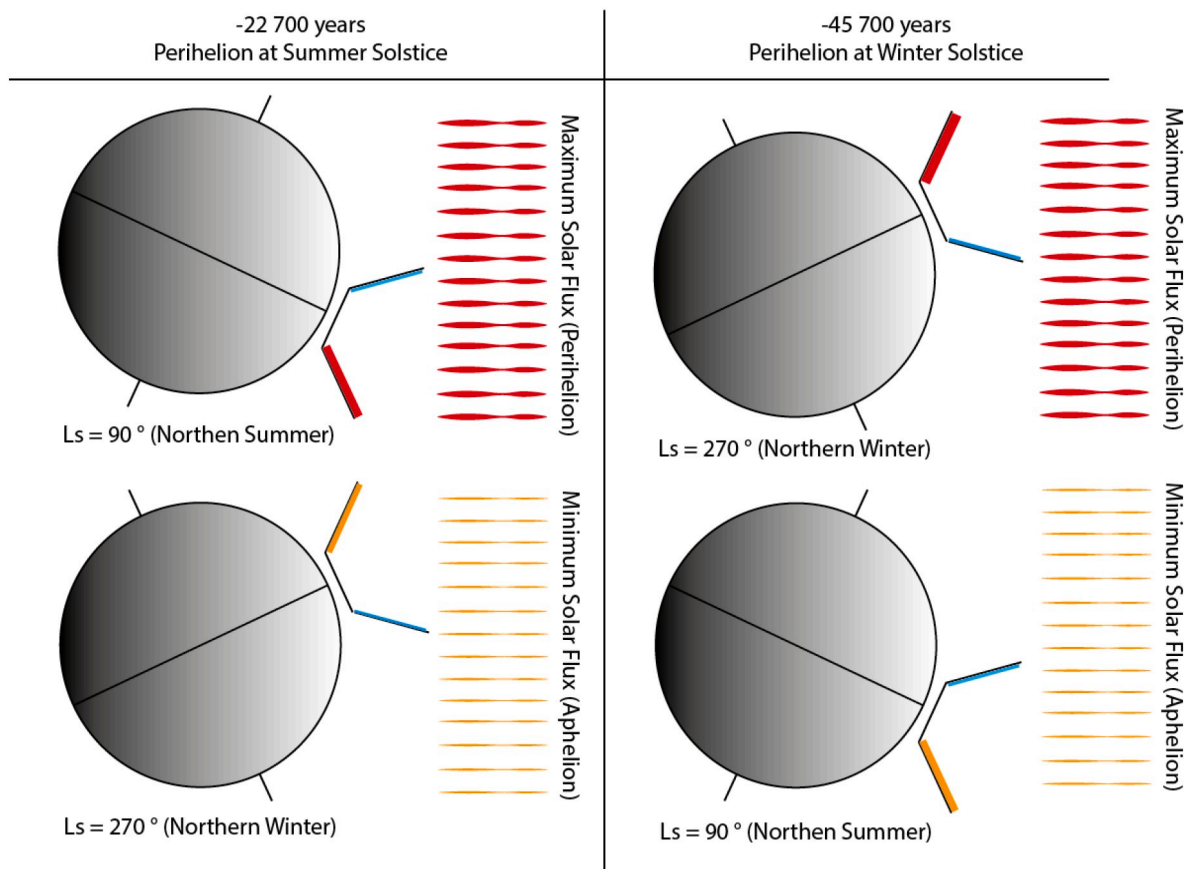


Fig. 8. Insolation received by a north- or south-facing slope located at the equator in two opposite cases. At 45.7 ka, the longitude of perihelion was very similar to the present day (Ls = 251°), south-facing slopes received maximum insolation. At 22.7 ka at the opposite sense of perihelion, north-facing slopes received maximum insolation at the equator.

9.4. Comparison with rockfall distribution

The insolation model was run at the latitude of each crater in this study, every 45° of solar longitude of perihelion, to cover a full precession cycle. To allow comparison with the rockfall distribution, we have binned insolation data with same method used for rockfall tracks (Section 3 – Fig. 4). The bins are then averaged for a specific latitude range and compared to a corresponding rockfall distribution for the same range. Results are plotted in Fig. 9. We find a significant linear correlation (Pearson $r = 0.69$; $R^2 = 0.48$; P -value $< .01$) between maximum diurnal insolation averaged for a full precession cycle and rockfall frequency (Fig. 9).

9.5. Insolation and thermal stress

Thermal stress is intrinsically higher where contrasts of temperature are greater, thus, one can expect it to be higher where solar flux is also higher. Molaro et al. (2015) state that the temporal gradient in temperature alone is a poor proxy for the thermal stress at the grain-scale and suggest using absolute temperatures and offset from diurnal means. The same conclusions are shared by Boelhouwers and Jonsson (2013), as well as Molaro and Byrne (2012). Solar flux and temperature are different physical quantities, but accurate temperature models are far more complex than insolation models and would make computation time for such a long timescale unmanageable. Also, temperature, including the peak temperature, is controlled by solar flux and the thermal properties of the material. Different rock compositions will have different thermal properties, which also affect the intensity of the thermal stress. However, one can expect thermal properties of rocks to be roughly the same within one crater, therefore only solar flux variations would control temperature differences between walls. The higher the solar flux received by a surface within a sol, the higher its maximum temperature, and the thermal stresses experienced by the material underneath it. Our results indicate a spatial correlation between maximum diurnal insolation (and potentially average daily temperature range) and rockfall frequency at the mid- and equatorial-latitudes (Fig. 9).

Overall, insolation is higher close to the equator than at the mid-latitudes, suggesting that thermal-related weathering should be more efficient there. This could provide an explanation for why we observe a lower median size of clasts (yet more numerous) at lower latitudes (Fig. 6).

These rockfalls could have occurred either during previous precession conditions and the track preserved or be recent rockfalls derived from bedrock weakened during previous precession conditions. The latter is more likely, as thermal stress is only responsible for preconditioning outcrops for rockfalls, not necessarily for triggering them (Fig. 1). Equatorial north-facing slopes could have been weathered in the past, but the rockfalls could then have occurred more recently. Hence, our results also indicate that the delay between weathering and rockfall is probably within the timeframe of recent orbital conditions (the last 100,000 years) as we have not found a signal of obliquity variations which have a longer timescale (e.g. $>10^\circ$ at >100 ka - Laskar et al., 2004). If rock breakdown occurred over similar timescales to obliquity cycles then, mid-latitude craters should have a similar frequency of rockfalls to equatorial craters because obliquity has changed from 15 to 45° in the last 10 Myrs (Laskar et al., 2004), meaning the location of maximum insolation transfers between the equator and the mid-latitudes. Assuming a relatively constant obliquity in the last 100 kyrs, reversed perihelion would not change insolation conditions to the point where a switch of maximum solar flux between north and south facing slopes would occur in the mid-latitudes, as it does at the equator, so no change in the rockfall distribution would be expected.

10. Conclusion

We report on the first detailed study of individual recent rockfalls in

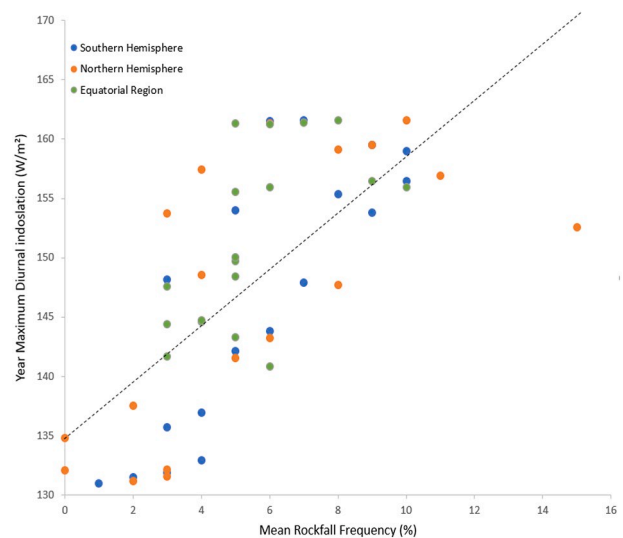


Fig. 9. Yearly maximum diurnal insolation plotted against normalized rockfall frequency in the northern hemisphere, southern hemisphere, and the equatorial region. Average diurnal insolation is computed for the latitude of each crater in a given range (between 50°S-15°S, 15°S-15°N and 15°N-40°N). The model runs for a whole martian year every 45° of solar longitude of perihelion, to have an average over a full precession cycle. The data are then binned the with same method used for the rockfall tracks (Section 3 – Fig. 4) and an average insolation value is obtained for the given latitude range. Solar data bins are compared to their corresponding normalized rockfall frequency bins (Fig. 4). P -value for the null-hypothesis is $\ll 0.01$.

impact craters on Mars inferred from the presence of tracks on the crater walls. We observe that the frequency of rockfalls and their orientation is dependent on latitude. The frequency of rockfall tracks is higher on the equator-facing slopes at the latitudes between 15°N/S and 40°N/50°S. In equatorial impact craters, the frequency of rockfall tracks is higher on both the north- and south-facing slopes compared to the east- and west-facing slopes (Fig. 4). Median clast size tends to decrease towards higher latitudes (Fig. 6). Topographic analysis shows that the signals observed are not a direct consequence of systematic variations in rock wall slopes (Fig. 7). Thus, these trends are more likely to be linked to the weathering mechanism responsible for rock breakdown prior to the rockfall rather than the slope inclination (Fig. 1). In addition, the observed patterns argue against a role of H₂O or CO₂ phase changes in preconditioning slopes for rockfalls, considering that most rockfalls occur in the equatorial area where these volatiles are scarce or lacking. Instead, thermal stress-driven subcritical cracking (Collins et al., 2018; Eppes and Keaini, 2017) related to high contrasts in surface temperature is more likely to be responsible for rock breakdown on modern Mars. Comparison between our results and a solar flux model (Fig. 9) emphasizes the potential role of diurnal temperature cycles at preconditioning slopes for rockfalls. We suggest that thermal stress must be developed over time-scales long enough for full cycles of precession to occur (Fig. 8) in order to explain the bimodal peaks in rockfall frequency at the equator.

Our study shows the key role of thermal stress in rock-breakdown on Mars. Thermal stress should thus be considered as an important factor in promoting mass-wasting process on impact crater walls.

Supplementary data to this article can be found online at <https://doi.org/10.1016/j.icarus.2019.113503>.

Acknowledgements

D. Mège, P.-A. Tesson, and J. Ciazela are supported by the TEAM program of the Foundation for Polish Science (TEAM/16-3/20) co-financed by the European Union under the European Regional Development Fund. J. Ciazela is additionally supported within the START

program of the Foundation for Polish Science. P-A Tesson, N. Mangold and S.J. Conway are also supported by CNES (French Space Agency). S.

R. Lewis gratefully acknowledges the support of the STFC/UK Space Agency under grants ST/R001405/1 and ST/S00145X/1.

Appendix A. Solar radiation model

Our model computes daily mean solar insolation for every pixel of the input Digital Terrain Model (DTM), at a specific sol and solar longitude (L_s). Each pixel has a slope and an aspect value as well as information about visibility in every direction (“viewshed”). Viewshed is computed for every pixel using *Skyline_3d* and *SkylineGraph_3d* function of *ArcPy* Python package for *ArcGIS* (Rich et al., 1994). Eqs. 1–8 making up the mathematical framework of our model are all extracted from Appelbaum and Flood, 1990.

Sun map calculation

Each sol is split in 48 equal timesteps, for which we calculate solar elevation angle (α_s) (Eq. 1) and Sun azimuth angle ϕ_s (Eq. 2).

$$\sin\alpha_s = \cos\omega\cos\delta\cos\varphi + \sin\delta\sin\varphi \quad (1)$$

$$\cos\phi_s = \frac{\sin\delta\cos\varphi - \cos\omega\cos\delta\sin\varphi}{\sin(\theta)} \quad (2)$$

where ω is the hour angle (Eq. 3), δ the solar declination (Eq. 4), φ is the latitude, and θ is the solar zenith angle ($\theta = 90^\circ - \alpha_s$). When $\omega < 0$, Sun azimuth angle should be subtracted from 180° . Hour angle can be obtained with the following equation:

$$\omega = 15 LST - 180 \quad (3)$$

where LST is the local solar time in Martian hours. 15° is the rotation speed of Mars per Martian hour.

Solar declination angle can be calculated using the following equation:

$$\sin\delta = \sin\delta_0\sin L_s \quad (4)$$

where δ_0 is Mars obliquity and L_s is the solar longitude. Comparison of Sun position in the sky at each step and visibility provided by the viewshed assess whether solar flux should be calculated or not.

Direct irradiance calculation

The solar constant S (W/m^2) is the solar flux received at the top of the atmosphere (Eq. 5).

$$S = S_{Mean} \left(\frac{1 + ecc \cos(L_s - L_{sp})}{1 - ecc^2} \right)^2 \quad (5)$$

where ecc is the eccentricity, L_s the solar longitude, L_{sp} solar longitude of perihelion and S_{Mean} the mean solar constant (for Mars: $586 \text{ W}/\text{m}^2$).

Direct solar radiation D (W/m^2) is the fraction of solar flux reaching the surface, and it is given by Eq. 6:

$$D = S e^{-\tau m(\theta)} \cos i \quad (6)$$

where τ is the optical depth of martian atmosphere, i the incidence angle (Eq. 8) and $m(\theta)$ the airmass which can be approximated by Eq. 7:

$$m(\theta) \cong \frac{1}{\cos\theta} \quad (7)$$

Slope correction

Incidence angle of the solar flux with respect to a tilted surface is calculated (Eq. 8) and included in Eq. 6.

$$\cos i = \cos\theta\cos G_z + \sin\theta\sin G_z\cos(\alpha_s - G_a) \quad (8)$$

where G_z is the slope inclination and G_a is the slope orientation.

References

- Appelbaum, J., Flood, D.J., 1990. Solar radiation on Mars. *Sol. Energy* 45 (6), 353–363. [https://doi.org/10.1016/0038-092X\(90\)90156-7](https://doi.org/10.1016/0038-092X(90)90156-7).
- Barlow, N.G., Bradley, T.L., 1990. Martian impact craters: correlations of ejecta and interior morphologies with diameter, latitude, and terrain. *Icarus* 87, 156–179. [https://doi.org/10.1016/0019-1035\(90\)90026-6](https://doi.org/10.1016/0019-1035(90)90026-6).
- Boelhouwers, J., Jonsson, M., 2013. Critical assessment of the 2°cmin^{-1} threshold for thermal stress weathering. *Geogr. Ann. Ser. A Phys. Geogr.* 95, 285–293. <https://doi.org/10.1111/geoa.12026>.
- Bourke, M.C., Edgett, K.S., Cantor, B.A., 2008. Recent aeolian dune change on Mars. *Geomorphology* 94, 247–255. <https://doi.org/10.1016/j.geomorph.2007.05.012>.
- Boynton, W.V., Feldman, W.C., Squyres, S.W., Prettyman, T.H., Brückner, J., Evans, L.G., Reedy, R.C., Starr, R., Arnold, J.R., Drake, D.M., et al., 2002. Distribution of

- hydrogen in the near surface of Mars: evidence for subsurface ice deposits. *Science* 297, 81–85. <https://doi.org/10.1126/science.1073722> (80-).
- Brown, J.R., Roberts, G.P., 2019. Possible evidence for variation in magnitude for marsquakes from fallen boulder populations, Grjota Valles, Mars. *Journal of Geophysical Research: Planets* 124 (3), 801–822. <https://doi.org/10.1029/2018JE005622>.
- Broxton, M.J., Edwards, L.J., 2008. The Ames stereo pipeline: Automated 3D surface reconstruction from orbital imagery. In: *Lunar and Planetary Science Conference*, p. 2419.
- Bruno, D.E., Ruban, D.A., 2017. Something more than boulders: a geological comment on the nomenclature of megaclasts on extraterrestrial bodies. *Planet. Space Sci.* 135, 37–42. <https://doi.org/10.1016/j.pss.2016.11.006>.
- Byrne, S., Dundas, C.M., Kennedy, M.R., Mellon, M.T., McEwen, A.S., Cull, S.C., Daubar, I.J., Shean, D.E., Seelos, K.D., Murchie, S.L., Cantor, B.A., Arvidson, R.E., Edgett, K.S., Reufer, A., Thomas, N., Harrison, T.N., Posiolova, L.V., Seelos, F.P., 2009. Distribution of mid-latitude ground ice on Mars from new impact craters. *Science* (80-) 325, 1674–1676. <https://doi.org/10.1126/science.1175307>.
- Carrozzo, F.G., Bellucci, G., Altieri, F., D'Aversa, E., Bibring, J.P., 2009. Mapping of water frost and ice at low latitudes on Mars. *Icarus* 203, 406–420. <https://doi.org/10.1016/j.icarus.2009.05.020>.
- Chevrier, V.F., Hanley, J., Altheide, T.S., 2009. Stability of perchlorate hydrates and their liquid solutions at the Phoenix landing site, Mars. *Geophys. Res. Lett.* 36 <https://doi.org/10.1029/2009GL037497>.
- Collins, B.D., Stock, G.M., 2016. Rockfall triggering by cyclic thermal stressing of exfoliation fractures. *Nat. Geosci.* 9, 395–400. <https://doi.org/10.1038/ngeo2686>.
- Collins, B.D., Stock, G.M., Eppes, M.C., Lewis, S.W., Corbett, S.C., Smith, J.B., 2018. Thermal influences on spontaneous rock dome exfoliation. *Nat. Commun.* 9 <https://doi.org/10.1038/s41467-017-02728-1>.
- Conway, S.J., Balme, M.R., 2014. Decimeter thick remnant glacial ice deposits on Mars. *Geophys. Res. Lett.* 41, 5402–5409. <https://doi.org/10.1002/2014GL060314>.
- Conway, S.J., Butcher, F.E.G., de Haas, T., Dejins, A.A.J., Grindrod, P.M., Davis, J.M., 2018. Glacial and gully erosion on Mars: a terrestrial perspective. *Geomorphol.* 318. <https://doi.org/10.1016/j.geomorph.2018.05.019>.
- Conway, S.J., Harrison, T.N., Soare, R.J., Britton, A.W., Steele, L.J., 2019. New slope-normalized global gully density and orientation maps for Mars. *Geol. Soc. Spec. Publ.* <https://doi.org/10.1144/SP467.3>.
- Corominas, J., Mavrouli, O., Ruiz-Carulla, R., 2017. Magnitude and frequency relations: are there geological constraints to the rockfall size? *Landslides* 15. <https://doi.org/10.1007/s10346-017-0910-z>.
- De Haas, T., Hauber, E., Kleinhans, M.G., 2013. Local late Amazonian boulder breakdown and denudation rate on Mars. *Geophys. Res. Lett.* <https://doi.org/10.1002/grl.50726>.
- Do Amaral Vargas, E., Velloso, R.Q., Chávez, L.E., Gusmão, L., Do Amaral, C.P., 2013. On the effect of thermally induced stresses in failures of some rock slopes in Rio de Janeiro, Brazil. *Rock Mech. Rock. Eng.* 46, 123–134. <https://doi.org/10.1007/s00603-012-0247-9>.
- Dundas, C.M., Bramson, A.M., Ojha, L., Wray, J.J., Mellon, M.T., Byrne, S., McEwen, A.S., Putzig, N.E., Viola, D., Sutton, S., Clark, E., Holt, J.W., 2018. Exposed subsurface ice sheets in the Martian mid-latitudes. *Science* (80-) 359, 199–201. <https://doi.org/10.1126/science.aao1619>.
- Eppes, M.C., Keanini, R., 2017. Mechanical weathering and rock erosion by climate-dependent subcritical cracking. *Rev. Geophys.* 55, 470–508. <https://doi.org/10.1002/2017RG000557>.
- Eppes, M.C., McFadden, L.D., Wegmann, K.W., Scuderi, L.A., 2010. Cracks in desert pavement rocks: further insights into mechanical weathering by directional insolation. *Geomorphology* 123, 97–108. <https://doi.org/10.1016/j.geomorph.2010.07.003>.
- Eppes, M.C., Willis, A., Molaro, J., Abernathy, S., Zhou, B., 2015. Cracks in Martian boulders exhibit preferred orientations that point to solar-induced thermal stress. *Nat. Commun.* 6, 6712. <https://doi.org/10.1038/ncomms7712>.
- Eppes, M.C., Magi, B., Hallet, B., Delmelle, E., Mackenzie-Helnwein, P., Warren, K., Swami, S., 2016. Deciphering the role of solar-induced thermal stresses in rock weathering. *Bull. Geol. Soc. Am.* 128, 1315–1338. <https://doi.org/10.1130/B31422.1>.
- Farmer, C.B., 1976. Liquid water on Mars. *Icarus* 28, 279–289. [https://doi.org/10.1016/0019-1035\(76\)90038-5](https://doi.org/10.1016/0019-1035(76)90038-5).
- Geissler, P.E., Sullivan, R., Golombek, M., Johnson, J.R., Herkenhoff, K., Bridges, N., Vaughan, A., Maki, J., Parker, T., Bell, J., 2010. Gone with the wind: Eolian erasure of the Mars rover tracks. *J. Geophys. Res.* 115 <https://doi.org/10.1029/2010je003674>.
- Gischig, V.S., 2016. Natural hazards: cracking cliffs feel the heat. *Nat. Geosci.* 9, 344–345. <https://doi.org/10.1038/ngeo2698>.
- Haberle, R.M., Grin, E.A., Zent, A.P., Quinn, R., McKay, C.P., Schaeffer, J., Cabrol, N.A., 2001. On the possibility of liquid water on present-day Mars. *J. Geophys. Res. E Planets* 106, 23317–23326. <https://doi.org/10.1029/2000JE001360>.
- Hall, K., 1999. The role of thermal stress fatigue in the breakdown of rock in cold regions. *Geomorphology* 47–63. [https://doi.org/10.1016/S0169-555X\(99\)00072-0](https://doi.org/10.1016/S0169-555X(99)00072-0).
- Hansen, C.J., Bourke, M., Bridges, N.T., Byrne, S., Colon, C., Dinega, S., Dundas, C., Herkenhoff, K., McEwen, A., Mellon, M., et al., 2011. Seasonal erosion and restoration of Mars' northern polar dunes. *Science* (80-) 331, 575–578.
- Harri, A.M., Genzer, M., Kemppinen, O., Gomez-Elvira, J., Haberle, R., Polkko, J., Savijärvi, H., Rennö, N., Rodriguez-Manfredi, J.A., Schmidt, W., Richardson, M., Siili, T., Paton, M., Torre-Juarez, M.D., Mäkinen, T., Newman, C., Rafkin, S., Mischina, M., Merikallio, S., Haukka, H., Martín-Torres, J., Komu, M., Zorzano, M.P., Peinado, V., Vazquez, L., Urqui, R., 2014. Mars science laboratory relative humidity observations: initial results. *J. Geophys. Res. E Planets* 119, 2132–2147. <https://doi.org/10.1002/2013JE004514>.
- Harrison, T.N., Osinski, G.R., Tornabene, L.L., Jones, E., 2015. Global documentation of gullies with the Mars reconnaissance orbiter context camera and implications for their formation. *Icarus* 252, 236–254. <https://doi.org/10.1016/j.icarus.2015.01.022>.
- Hecht, M.H., 2002. Metastability of liquid water on Mars. *Icarus* 156, 373–386. <https://doi.org/10.1006/icar.2001.6794>.
- Herrick, R.R., Hessen, K.K., 2006. The planforms of low-angle impact craters in the northern hemisphere of Mars. *Meteorit. Planet. Sci.* 41, 1483–1495. <https://doi.org/10.1111/j.1945-5100.2006.tb00431.x>.
- James, P.B., Hansen, G.B., Titus, T.N., 2005. The carbon dioxide cycle. *Adv. Sp. Res.* 35, 14–20. <https://doi.org/10.1016/j.asr.2003.04.056>.
- Keefer, D.K., 1984. Landslides caused by earthquakes. *Geol. Soc. Am. Bull.* 95, 406–421. [https://doi.org/10.1130/0016-7606\(1984\)95<406:LCBE>2.0.CO;2](https://doi.org/10.1130/0016-7606(1984)95<406:LCBE>2.0.CO;2).
- Kelly, N.J., Boynton, W.V., Kerry, K., Hamara, D., Janes, D., Reedy, R.C., Kim, K.J., Haberle, R.M., 2006. Seasonal polar carbon dioxide frost on Mars: CO₂ mass and columnar thickness distribution. *J. Geophys. Res.* 112 <https://doi.org/10.1029/2006je002678>.
- Kreslavsky, M.A., Head, J.W., 2002. Mars: nature and evolution of young latitude-dependent water-ice-rich mantle. *Geophys. Res. Lett.* 29, 14. <https://doi.org/10.1029/2002gl015392>.
- Kreslavsky, M.A., Head, J.W., 2003. North-south topographic slope asymmetry on Mars: evidence for insolation-related erosion at high obliquity. *Geophys. Res. Lett.* 30 <https://doi.org/10.1029/2003gl017795>.
- Kreslavsky, M.A., Head, J.W., 2018. Mars climate history: insights from impact Crater Wall slope statistics. *Geophys. Res. Lett.* 45, 1751–1758. <https://doi.org/10.1002/2017GL075663>.
- Krishna, N., Kumar, P.S., 2016. Impact spallation processes on the moon: a case study from the size and shape analysis of ejecta boulders and secondary craters of Censorinus crater. *Icarus* 264, 274–299. <https://doi.org/10.1016/j.icarus.2015.09.033>.
- Kumar, P.S., 2005. Structural effects of meteorite impact on basalt: evidence from Lonar crater, India. *J. Geophys. Res. Solid Earth* 110, 1–10. <https://doi.org/10.1029/2005JB003662>.
- Kumar, P.S., Kring, D.A., 2008. Impact fracturing and structural modification of sedimentary rocks at meteor crater, Arizona. *J. Geophys. Res.* 113 <https://doi.org/10.1029/2008JE003115>.
- Kumar, P.S., Sruthi, U., Krishna, N., Lakshmi, K.J.P., Menon, R., Amitabh, Krishna, B.G., Kring, D.A., Head, J.W., Goswami, J.N., Kumar, A.S.K., 2016. Recent shallow moonquake and impact-triggered boulder falls on the moon: new insights from the Schrödinger basin. *J. Geophys. Res. Planets* 121, 147–179. <https://doi.org/10.1002/2015je004850>.
- Senthil Kumar, P., Krishna, N., Prasanna Lakshmi, K.J., Raghukanth, S.T.G., Dhabu, A., Platz, T., 2019. Recent seismicity in Valles Marineris, Mars: insights from young faults, landslides, boulder falls and possible mud volcanoes. *Earth Planet. Sci. Lett.* 505, 51–64. <https://doi.org/10.1016/j.epsl.2018.10.008>.
- Lamp, J.L., Marchant, D.R., Mackay, S.L., Head, J.W., 2017. Thermal stress weathering and the spalling of Antarctic rocks. *J. Geophys. Res. Earth Surf.* 122, 3–24. <https://doi.org/10.1002/2016jf003992>.
- Laskar, J., Correia, A.C.M., Gastineau, M., Joutel, F., Levrard, B., Robutel, P., 2004. Long term evolution and chaotic diffusion of the insolation quantities of Mars. *Icarus* 170, 343–364. <https://doi.org/10.1016/j.icarus.2004.04.005>.
- Lucchitta, B.K., 1978. A large landslide on Mars. *Geol. Soc. Am. Bull.* 89, 1601. [https://doi.org/10.1130/0016-7606\(1978\)89<1601:ALLOM>2.0.CO;2](https://doi.org/10.1130/0016-7606(1978)89<1601:ALLOM>2.0.CO;2).
- Malin, M.C., Bell, J.F., Cantor, B.A., Caplinger, M.A., Calvin, W.M., Clancy, R.T., Edgett, K.S., Edwards, L., Haberle, R.M., James, P.B., Lee, S.W., Ravine, M.A., Thomas, P.C., Wolff, M.J., 2007. Context camera investigation on board the Mars reconnaissance orbiter. *J. Geophys. Res.* 112, E05S04. <https://doi.org/10.1029/2006JE002808>.
- Mavrouli, O., Corominas, J., Jaboyedoff, M., 2015. Size distribution for potentially unstable rock masses and in situ rock blocks using LIDAR-generated digital elevation models. *Rock Mech. Rock. Eng.* 48, 1589–1604. <https://doi.org/10.1007/s00603-014-0647-0>.
- McEwen, A.S., Eliason, E.M., Bergstrom, J.W., Bridges, N.T., Hansen, C.J., Delamere, W. A., Grant, J.A., Gulick, V.C., Herkenhoff, K.E., Keszthelyi, L., Kirk, R.L., Mellon, M.T., Squyres, S.W., Thomas, N., Weitz, C.M., 2007. Mars reconnaissance Orbiter's high resolution imaging science experiment (HiRISE). *J. Geophys. Res.* 112, E05S02. <https://doi.org/10.1029/2005JE002605>.
- McKay, C.P., Molaro, J.L., Marinova, M.M., 2009. High-frequency rock temperature data from hyper-arid desert environments in the Atacama and the Antarctic dry valleys and implications for rock weathering. *Geomorphology* 110, 182–187. <https://doi.org/10.1016/j.geomorph.2009.04.005>.
- Mellon, M.T., 1997. Small-scale polygonal features on Mars: seasonal thermal contraction cracks in permafrost. *J. Geophys. Res. Planets* 102, 25617–25628. <https://doi.org/10.1029/97JE02582>.
- Mellon, M.T., Arvidson, R.E., Sizemore, H.G., Searls, M.L., Blaney, D.L., Cull, S., Hecht, M.H., Heet, T.L., Keller, H.U., Lemmon, M.T., Markiewicz, W.J., Ming, D.W., Morris, R.V., Pike, W.T., Zent, A.P., 2009. Ground ice at the Phoenix landing site: stability state and origin. *J. Geophys. Res.* 114, E00E07. <https://doi.org/10.1029/2009JE003417>.
- Melosh, H.J., 1989. Impact cratering: A geologic process. In: *Oxford Monographs on Geology and Geophysics*, No. 11.
- Melosh, H.J., Ivanov, B.A., 1999. Impact crater collapse. *Annu. Rev. Earth Planet. Sci.* 27, 385–415. <https://doi.org/10.1146/annurev.earth.27.1.385>.

- Molaro, J., Byrne, S., 2012. Rates of temperature change of airless landscapes and implications for thermal stress weathering. *J. Geophys. Res. E Planets* 117. <https://doi.org/10.1029/2012JE004138>.
- Molaro, J.L., Byrne, S., Langer, S.A., 2015. Grain-scale thermoelastic stresses and spatiotemporal temperature gradients on airless bodies, implications for rock breakdown. *J. Geophys. Res. Planets* 120, 255–277. <https://doi.org/10.1002/2014JE004729>.
- Molaro, J.L., Byrne, S., Le, J.L., 2017. Thermally induced stresses in boulders on airless body surfaces, and implications for rock breakdown. *Icarus* 294, 247–261. <https://doi.org/10.1016/j.icarus.2017.03.008>.
- Moore, H.J., Hutton, R.E., Clow, G.D., Spitzer, C.R., 1987. Physical properties of the surface materials at the Viking landing sites on Mars. *US Geol. Surv. Prof. Pap.* <https://doi.org/10.3133/pp1389>.
- Mouginot, J., Pommerol, A., Kofman, W., Beck, P., Schmitt, B., Herique, A., Grima, C., Safaenili, A., Plaut, J.J., 2010. The 3–5MHz global reflectivity map of Mars by MARSIS/Mars express: implications for the current inventory of subsurface H₂O. *Icarus* 210, 612–625. <https://doi.org/10.1016/j.icarus.2010.07.003>.
- Nara, Y., Kashiwaya, K., Nishida, Y., Ii, T., 2017. Influence of surrounding environment on subcritical crack growth in marble. *Tectonophysics* 706–707, 116–128. <https://doi.org/10.1016/j.tecto.2017.04.008>.
- Neumann, G.A., 2003. Mars orbiter laser altimeter pulse width measurements and footprint-scale roughness. *Geophys. Res. Lett.* 30 <https://doi.org/10.1029/2003gl017048>.
- Ojha, L., Chojnacki, M., McDonald, G.D., Shumway, A., Wolff, M.J., Smith, M.D., McEwen, A.S., Ferrier, K., Huber, C., Wray, J.J., Toigo, A., 2017. Seasonal slumps in Juventae Chasma, Mars. *J. Geophys. Res. Planets* 122, 2193–2214. <https://doi.org/10.1002/2017je005375>.
- Piqueux, S., Kleinböhl, A., Hayne, P.O., Heavens, N.G., Kass, D.M., McCleese, D.J., Schofield, J.T., Shirley, J.H., 2016. Discovery of a widespread low-latitude diurnal CO₂ frost cycle on Mars. *J. Geophys. Res. Planets* 121, 1174–1189. <https://doi.org/10.1002/2016JE005034>.
- Rich, P.M., Dubayah, R., Hetrick, W.A., Saving, S.C., Dubayah, R.O., 1994. Using Viewshed models to calculate intercepted solar radiation: applications in ecology. *Am. Soc. Photogramm. Remote Sens. Tech. Pap.* 524–529.
- Robbins, S.J., Hynek, B.M., 2012. A new global database of Mars impact craters ≥ 1 km: 2. Global crater properties and regional variations of the simple-to-complex transition diameter. *J. Geophys. Res. Planets* 117. <https://doi.org/10.1029/2011JE003967>.
- Roberts, G.P., Matthews, B., Bristow, C., Guerrieri, L., Vetterlein, J., 2012. Possible evidence of paleomarsquakes from fallen boulder populations, Cerberus Fossae, Mars. *J. Geophys. Res. Planets* 117. <https://doi.org/10.1029/2011JE003816>.
- Santana, D., Corominas, J., Mavrouli, O., Garcia-Sellés, D., 2012. Magnitude–frequency relation for rockfall scars using a terrestrial laser scanner. *Eng. Geol.* 145–146, 50–64. <https://doi.org/10.1016/j.enggeo.2012.07.001>.
- Schmidt, F., Andrieu, F., Costard, F., Kocifaj, M., Meresescu, A.G., 2017. Formation of recurring slope lineae on Mars by rarefied gas-triggered granular flows. *Nat. Geosci.* 10, 270–273. <https://doi.org/10.1038/ngeo2917>.
- Schorghofer, N., Edgett, K.S., 2006. Seasonal surface frost at low latitudes on Mars. *Icarus* 180, 321–334. <https://doi.org/10.1016/j.icarus.2005.08.022>.
- Selby, M.J., et al., 1982. *Hillslope Materials and Processes*. Oxford Univ. Press.
- Senthil Kumar, P., Prasanna Lakshmi, K.J., Krishna, N., Menon, R., Sruthi, U., Keerthi, V., Senthil Kumar, A., Mysaiah, D., Seshunarayana, T., Sen, M.K., 2014. Impact fragmentation of Lonar crater, India: implications for impact cratering processes in basalt. *J. Geophys. Res. E Planets* 119, 2029–2059. <https://doi.org/10.1002/2013JE004543>.
- Smith, M.D., 2002. The annual cycle of water vapor on Mars as observed by the Thermal Emission Spectrometer. *J. Geophys. Res. Planets* 107. <https://doi.org/10.1029/2001JE001522>, 25–1–25–19.
- Spanovich, N., Smith, M.D., Smith, P.H., Wolff, M.J., Christensen, P.R., Squyres, S.W., 2006. Surface and near-surface atmospheric temperatures for the Mars exploration rover landing sites. *Icarus* 180, 314–320. <https://doi.org/10.1016/j.icarus.2005.09.014>.
- Sullivan, R., Banfield, D., Bell, J.F., Calvin, W., Fike, D., Golombek, M., Greeley, R., Grotzinger, J., Herkenhoff, K., Jerolmack, D., Malin, M., Ming, D., Soderblom, L.A., Squyres, S.W., Thompson, S., Watters, W.A., Weitz, C.M., Yen, A., 2005. Aeolian processes at the Mars exploration rover Meridiani Planum landing site. *Nature* 436, 58–61. <https://doi.org/10.1038/nature03641>.
- Sullivan, R., Arvidson, R., Bell, J.F., Gellert, R., Golombek, M., Greeley, R., Herkenhoff, K., Johnson, J., Thompson, S., Whelley, P., Wray, J., 2008. Wind-driven particle mobility on Mars: Insights from Mars exploration rover observations at “El Dorado” and surroundings at Gusev crater. *J. Geophys. Res.* 113, E06S07. <https://doi.org/10.1029/2008JE003101>.
- Terzaghi, K., 1962. Stability of steep slopes on hard Unweathered rock. *Géotechnique* 12, 251–270. <https://doi.org/10.1680/geot.1962.12.4.251>.
- Tsige, M., Ruiz, J., del Río, I.A., Jiménez-Díaz, A., 2016. Modeling of landslides in Valles Marineris, Mars, and implications for initiation mechanism. *Earth. Moon. Planets* 118, 15–26. <https://doi.org/10.1007/s11038-016-9488-z>.
- Viles, H., Ehlmann, B., Wilson, C.F., Cebula, T., Page, M., Bourke, M., 2010. Simulating weathering of basalt on Mars and earth by thermal cycling. *Geophys. Res. Lett.* 37 <https://doi.org/10.1029/2010GL043522>.
- Vincendon, M., Forget, F., Mustard, J., 2010. Water ice at low to midlatitudes on Mars. *J. Geophys. Res.* 115, E10001 <https://doi.org/10.1029/2010JE003584>.
- Vincendon, M., Mustard, J., Forget, F., Kreslavsky, M., Spiga, A., Murchie, S., Bibring, J.-P., 2010. Near-tropical subsurface ice on Mars. *Geophys. Res. Lett.* 37 <https://doi.org/10.1029/2009GL041426>.
- Warren, K., Eppes, M.-C., Swami, S., Garbini, J., Putkonen, J., 2013. Automated field detection of rock fracturing, microclimate, and diurnal rock temperature and strain fields. *Geosci. Instrumentation, Methods Data Syst.* 2, 275–288. <https://doi.org/10.5194/gi-2-275-2013>.